A LOW-RESOLUTION ADC PROOF-OF-CONCEPT DEVELOPMENT FOR A FULLY-DIGITAL MILLIMETER-WAVE JOINT COMMUNICATION-RADAR

Preeti Kumari[1]*, Amine Mezghani*[2]*, and Robert W. Heath, Jr.*[1]

[1] The University of Texas at Austin, TX, USA, email: {preeti_kumari, rheath}@utexas.edu
[2] University of Manitoba, Canada, amine.mezghani@umanitoba.ca

ABSTRACT

A fully-digital mmWave wideband JCR places difficult demands of power consumption and hardware complexity on the receivers' analog-to-digital converters (ADCs). To address these concerns, we present a low-complexity proof-of-concept (PoC) development for a wideband MIMO JCR that uses a mmWave communications waveform and low-resolution ADCs, while maintaining a separate radio-frequency chain per antenna. To accurately characterize the radar performance of our developed PoC tested, we conduct experiments using a trihedral corner reflector and apply traditional as well as advanced receiver processing algorithms. The results demonstrate that our MIMO PoC platform with a fully-digital JCR waveform at 73 GHz carrier frequency, 2 GHz bandwidth, and 1-bit ADCs achieves high range/direction estimation accuracy as well as high detection capability with a wide field of view.

1. INTRODUCTION

A millimeter-wave (mmWave) MIMO technology with high-speed analog-to-digital converters (ADCs) will enable high performance and design flexibility for joint communication and radar (JCR) due to the wide bandwidth, high dimensions, and fully-digital baseband processing [1]. The use of high-speed, high-resolution ADCs in these JCRs, however, will result in huge power consumption and high hardware complexity [2]. Therefore, a low-resolution quantized receiver will enable a practical fully-digital mmWave JCR solution for futuristic portable devices [3] and autonomous vehicles [4].

There is some work on MIMO communications for low-resolution ADCs with a high sampling rate [5–7]. In [6], an iterative channel estimation method using Expectation Maximization (EM) was proposed for the ultra-high frequency band. To leverage the sparsity in the mmWave channels, a generalized approximate message passing (GAMP)-based channel estimation algorithm was proposed and numerically analyzed in [7]. They [5–7], however, did not consider the self-interference effect. There is limited work on low-resolution ADCs for a full-duplex radar that transmits and receives simultaneously. In [8, 9], time-varying thresholds and ℓ_1-norm minimization was proposed for a single-input-single-output radar with 1-bit ADC. To realize a fully-digital wideband mmWave JCR, [10, 11] proposed the use of high-speed, low-resolution ADCs receivers. The Cramér Rao bounds demonstrated that the radars with 1-bit ADC perform closely to the infinite-bit ADC for a single-target scenario at low signal-to-noise ratio (SNR) [10, 11].

In this paper, we present a proof-of-concept (PoC) for a fully-digital JCR system with high-speed, low-resolution ADCs using real channel measurements at 71-76 GHz band with 2 GHz bandwidth. In our recent paper [12], we have described our wideband mmWave MIMO JCR platform with communication-centric waveforms and high-resolution ADCs. In this paper, we experimentally evaluate the performance of a fully-digital JCR with low-resolution quantized receiver architecture proposed in [10] using emulations on the channel measured from our testbed in [12]. To perform radar characterization of our low-resolution communication-centric JCR PoC platform, we conduct experiments using a trihedral corner reflector and apply GAMP algorithm for receiver processing. To our knowledge, this is the first experimental evaluation of a wideband fully-digital mmWave MIMO radar with high-speed, low-resolution ADCs. Our PoC platform with low-resolution ADCs demonstrates the high-resolution sensing capability of the communication-centric JCR system with a wide field-of-view.

Notation: The operator $(\cdot)^{\mathrm{T}}$ denote transpose of a matrix. The quantization function $\mathcal{Q}(\cdot)$ is applied componentwise and separately to the real and imaginary parts.

2. SYSTEM MODEL AND DSP ALGORITHMS

In this section, we present the theoretical background and assumptions pertaining to the development of radar digital sig-

This material is based upon work supported in part by the National Science Foundation under Grant No. ECCS-1711702 and the U.S. Department of Transportation through the Data-Supported Transportation Operations and Planning (D-STOP) Tier 1 University Transportation Center.

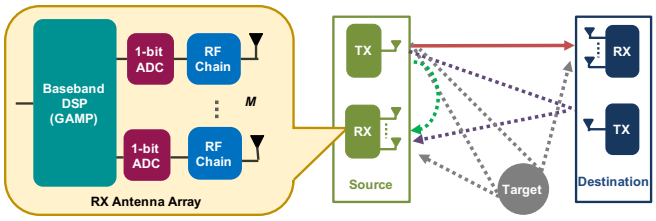

Fig. 1. A fully-digital joint communication-radar, where the communication and radar receivers use low-resolution ADCs per receive RF chain to reduce the hardware complexity.

nal processing (DSP) receiver algorithms for our mmWave JCR PoC platform with high-speed, low-resolution ADCs and communication-centric waveform. Although some hardware impairments, like zero phase noise and power amplifier linearity, are not incorporated in the system model described in this section, they will be taken into account in our experimental PoC evaluation. As a first step to investigate the feasibility of a mmWave JCR system with low-resolution ADCs, we assume a static indoor setting. This can be extended to dynamic scenarios by incorporating the Doppler effect.

Consider a full-duplex source that transmits a JCR waveform to a communication receiver at the destination, while simultaneously receiving and processing the echoes from the surrounding targets and clutter for radar sensing. The receiver employs an M element uniform linear array with low-resolution ADCs per radio-frequency (RF) chain. The transmit (TX) and receive (RX) antennas at the source are kept as far as possible to reduce the self-interference due to the full-duplex operation, while making sure that the observed range and direction of a target is the same.

In a T second coherent processing interval, we consider a single carrier physical layer TX JCR waveform with μ fraction of preamble symbols and $1-\mu$ fraction of communication data symbols. Similar to [13], we exploit the training sequences used in the preamble for radar sensing due to its good autocorrelation properties. We assume that the training sequences posses good correlation properties for a low-resolution radar and has a low peak-to-average power ratio [7]. The preamble is denoted by an N-element vector $\mathbf{t} \in \mathbb{C}^{N\times 1}$. The mmWave WLAN standard [14] with Golay complementary sequences and 5G experimental testbed [15] with Zadoff-Chu sequence can realize this JCR frame structure.

We represent the radar channel in the range and azimuth angle domain [16]. Assuming there are L range bins, we denote the channel coefficient vector corresponding to the ℓ^{th} range bin as $\mathbf{x}_\ell \in \mathbb{C}^M$ and the channel coefficient vector corresponding to LM range-angle cells as $\mathbf{x} = [\mathbf{x}_0^{\mathrm{T}}, \cdots, \mathbf{x}_{\mathrm{L}-1}^{\mathrm{T}}]^{\mathrm{T}}$, which consist of direct-path and multi-path reflections from near-by targets and clutter along with the residual self-interference, as shown in Fig. 1. Denoting $\mathbf{w}$ as the noise vector with variance σ_w^2, $\mathbf{F}_{\mathrm{M}} \in \mathbb{C}^{M\times M}$ as the DFT matrix, and $\mathbf{G} \in \mathbb{C}^{L\times N}$ as the circulant-shift matrix of $\mathbf{t}$ with the ℓ^{th} row obtained by circularly shifting $\mathbf{t}$ by ℓ, the quantized complex-baseband received radar signal $\mathbf{y} \in \mathbb{C}^{MN\times 1}$ can be represented as

$$\mathbf{y} = \mathcal{Q}\Big((\mathbf{G}^{\mathrm{T}} \otimes \mathbf{F}_{\mathrm{M}})\mathbf{x} + \mathbf{w}\Big). \tag{1}$$

We define the SNR as $\mathbb{E}\left[||\mathbf{z}||^2\right]/\sigma_w^2$, where $\mathbf{z} = (\mathbf{G}^{\mathrm{T}} \otimes \mathbf{F}_{\mathrm{M}})\mathbf{x}$ is the unquantized noiseless signal vector. For radar performance evaluation, we consider the extreme case of only 1-bit ADC and compare it with 12-bit resolution ADC used in our JCR testbed [12]. The main advantage of this architecture is that the 1-bit ADC is just a simple comparator and can be implemented with very low power consumption and reduced the overall complexity of the circuit [17].

Algorithm 1 Min-sum-GAMP algorithm

Input: observation vector $\mathbf{y}$, $\mathbf{A} = \mathbf{G}^{\mathrm{T}} \otimes \mathbf{F}_{\mathrm{M}}$
Initialize: $\mathbf{z}^0 = \mathbf{0}$, $\mathbf{x}^0 = \mathbf{0}$, $\boldsymbol{\theta}^0 = \text{const}$, $\ell \leftarrow 0$
repeat
  $\ell \leftarrow \ell + 1$
  Output Step:
  $\mathbf{z}^\ell \leftarrow g_\ell(-\mathbf{A}\hat{\mathbf{x}}^{\ell-1} + \boldsymbol{\theta}^{\ell-1} \circ \mathbf{z}^{\ell-1}, \mathbf{y}, \boldsymbol{\theta}^{\ell-1})$
  $\boldsymbol{\xi}^\ell \leftarrow (\mathbf{A} \circ \mathbf{A}^*)^{\mathrm{T}} g'_\ell(-\mathbf{A}\hat{\mathbf{x}}^{\ell-1} + \boldsymbol{\theta}^{\ell-1} \circ \mathbf{z}^{\ell-1}, \boldsymbol{\theta}^{\ell-1}, \mathbf{y})$
  Input Step:
  $\mathbf{x}^\ell \leftarrow f_\ell(\mathbf{A}^{\mathrm{H}}\mathbf{z}^\ell + \boldsymbol{\xi}^\ell \circ \hat{\mathbf{x}}^{\ell-1}, \boldsymbol{\xi}^\ell)$
  $\boldsymbol{\theta}^\ell \leftarrow (\mathbf{A} \circ \mathbf{A}^*) f'_\ell(\mathbf{A}^{\mathrm{H}}\mathbf{z}^\ell + \boldsymbol{\xi}^\ell \circ \hat{\mathbf{x}}^{\ell-1}, \boldsymbol{\xi}^\ell)$
until the cost does not significantly decrease or a maximum iteration count has been reached
return $\mathbf{x}^\ell$.

In Algorithm 1, we provide the pseudo-code of GAMP algorithm [18] to estimate $\mathbf{x}$ based on the quantized observation $\mathbf{y}$. The recursive approach breaks apart the entire estimation problem into smaller scalar estimations described by the input denoising function [19]

$$f_\ell(v, \xi^\ell) = \mathrm{e}^{\mathrm{j}\angle v} \max\left(|v| - \lambda, 0\right)/\xi^\ell, \tag{2}$$

for the sparse reconstruction with a certain regularization parameter λ, and the output (residual) function (applied element-wise for each real/imaginary component) [19]

$$g_\ell(-u, y, \theta^\ell) = \frac{\exp\left(-\frac{(y^{\mathrm{lo}}-u)^2}{\sigma_w^2+\theta^\ell}\right) - \exp\left(-\frac{(y^{\mathrm{up}}-u)^2}{\sigma_w^2+\theta^\ell}\right)}{2\sqrt{\pi(\sigma_w^2+\theta^\ell)}\left(\mathrm{erf}\left(\frac{y^{\mathrm{up}}-u}{\sqrt{\sigma_w^2+\theta^\ell}}\right) - \mathrm{erf}\left(\frac{y^{\mathrm{low}}-u}{\sqrt{\sigma_w^2+\theta^\ell}}\right)\right)} - \frac{u}{\theta^\ell}, \tag{3}$$

with y^{lo} and y^{up} being the lower and upper quantization boundary. The scalar functions f_ℓ and g_ℓ are applied element-wise to vectors in the GAMP algorithm. The corresponding Wirtinger derivatives $\boldsymbol{\xi}^\ell$ and $\boldsymbol{\theta}^\ell$ are obtained with respect to the first argument.

3. PROOF-OF-CONCEPT JCR PLATFORM

In this section, we describe both the hardware [12] and the software platform for our PoC development of a fully-digital mmWave JCR with low-resolution ADCs per RF chain.

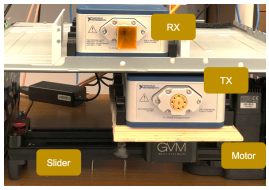

Fig. 2. The SIMO JCR hardware platform, where the sliding motor is used to synthesize multiple digital RF chains.

Our fully-digital JCR hardware platform operates at 71-76 GHz band, has 2 GHz bandwidth with 1.536 GHz sampling rate, employs 12-bit ADC with 3.072 GSps, and uses a sliding rail of 21 cm. The single-input-multiple-output (SIMO) mmWave JCR channel sounding platform is synthesized by moving TX antenna on a slider using a stepper motor to simultaneously collect RX signals with multiple TX-RX inter-spacing for communication and radar receivers, as shown in Fig. 2. For each TX-RX inter-spacing, the transmitter sends several continuous training sequences at 73 GHz and then wait for a predefined time interval to avoid any range ambiguity. The inter-distance between any two consecutive TX locations is 1.69 mm, which is less than half of the carrier wavelength and aids in avoiding any grating lobes as well as enables a good beamforming shape. For performance evaluation of the mmWave JCR system with low-resolution ADCs per antenna, we use our time-division multiplexing SIMO JCR testbed at the mmWave band for static MIMO radar testing. This testbed, however, can be extended for dynamic scenarios using smaller time intervals between steps with sophisticated hardware enhancements and advanced processing such as used in inverse synthetic aperture radar.

The training sequence used in our mmWave JCR testbed is Zadoff-Chu sequence of length $N = 2048$. The raw signal $\mathbf{y}$ received from our real-time JCR sounding testbed is used for evaluating the performance of low-resolution quantized radar receiver offline through emulations. We employ traditional FFT-based processing for high-resolution quantized receiver, where we first estimate the channel in the range-domain for each antenna location and then apply FFT in the angle domain for each range bin. We also use advanced sparse reconstruction using the GAMP algorithm in Algorithm 1 with Gaussian mixture (GM) model assumption of the channel coefficients $\mathbf{x}$ to estimate the radar channel in range-angle domain. To optimize the hyperparameter used in the GAMP algorithm such as the GM parameters and noise variance, we use expectation-maximization [20].

4. EXPERIMENTAL RESULTS

In this section, we describe the experiment conducted using our testbed for the performance evaluation of JCR with low-resolution ADCs. We perform testing using a trihedral corner reflector placed in the indoor lab, as shown in Fig. 3.

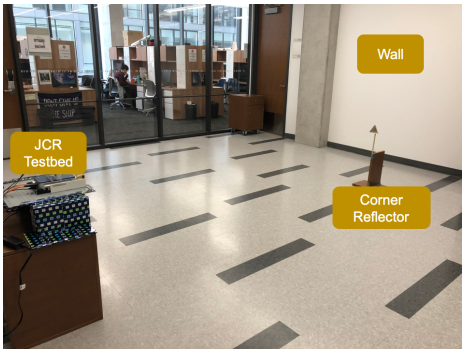

Fig. 3. Experimental setup for radar channel measurement using our mmWave JCR testbed.

To evaluate the radar performance of our JCR testbed in the range-angle domain, we placed a corner reflector of 0.1 m edge length at 3.216 m and 30°, and moved the TX with $M = 86$ steps. For benchmarking purposes, we measured the target distance and angle using a laser device with mm-level accuracy. Fig. 4(a) shows the normalized radar channel measured using our JCR sounding testbed and FFT-based traditional processing on the received signal collected by sending several repeated training sequences. We used the tap corresponding to the self-interference effect in the channel estimate obtained at the first antenna location as the zero range reference. We found the tap corresponding to the corner reflector to be at a constant distance with respect to the zero reference for all M steps, while its magnitude varied within 1 dB. From Fig. 4(a), we see that the corner reflector is at 3.223 m and 31°, demonstrating high-resolution sensing capability of our testbed. We also observe wall reflection near 4.9 m and several multipath reflections around it. The wall reflection is stronger than the corner reflector because it has a larger radar cross-section and because the corner reflector was placed quite far from the boresight resulting in smaller antenna gain.

To investigate the performance of our JCR testbed with high- and low- resolution ADCs and GAMP algorithm at low SNR for the same radar channel in Fig. 4(a), we use emulations on the collected received signal. We emulate the received signal in (1) using the channel in Fig. 4(a) as $\mathbf{x}$, the Zadoff-Chu sequence of $N = 512$ length as $\mathbf{t}$, and an additional additive white Gaussian noise to decrease the SNR to five. We further apply no quantization or 1-bit quantization on the emulated received signal. Fig. 4(b) shows the radar image obtained using GAMP algorithm on the emulated re-

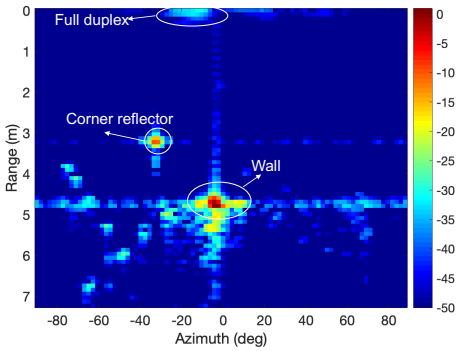

(a) FFT-based

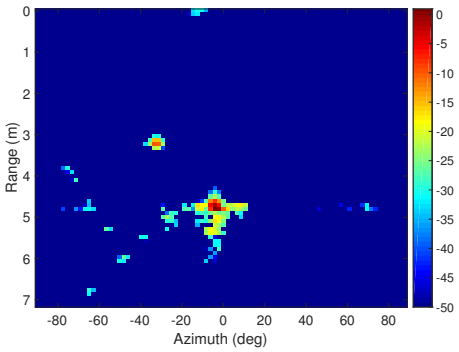

(b) GAMP-based

Fig. 4. Radar image in dB scale estimated using high-resolution ADC in presence of the self-interference effect. The channel estimate in (b) has reduced sidelobes than (a).

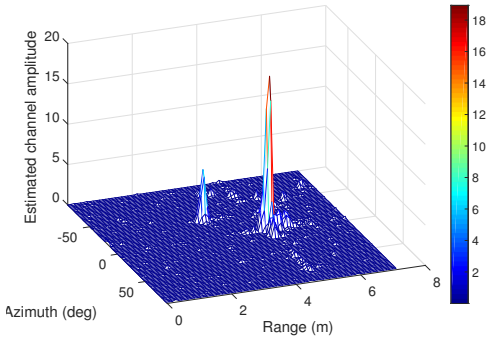

(a) 3-D mesh plot in linear scale

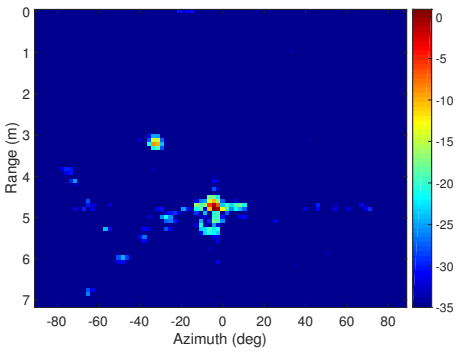

(b) 2-D range-azimuth image in dB scale

Fig. 5. Radar channel estimated using GAMP processing with 1-bit ADC. In the estimated radar image, the target corner reflector appears distortionless and there is no false alarm.

ceived signal for 12-bit ADC quantization employed in the NI mmWave testbed. Although Fig. 4(b) is observed at lower SNR, we see that Fig. 4(b) has reduced sidelobes than the FFT-based radar image in Fig. 4(b). It detects the full-duplex effect, corner reflector, as well as the wall without any false detections. The computational complexity although is higher than the FFT-based processing.

Figs. 5(a) and (b) shows the 3-D mesh plot and 2-D image of the normalized radar channel estimated using the emulated received signal with 1-bit ADC and GAMP processing. The corner reflector target in the radar image appears distortionless in Figs. 5(a) and (b). The full-duplex effect and the wall is detectable in Fig. 5(b) without any false detections and has reduced sidelobes than the FFT-based processing in Fig. 4(a). Below 35 dB, however, we observe some false detection in Fig. 5(a). The dynamic range seems to decrease from 50 dB to 35 dB as compared to the high-resolution case in Fig. 4(b). The performance of 1-bit ADC, however, can be further improved by using longer training sequences or more antennas. The closeness of 1-bit ADC radar image with 12-bit ADC radar image will be further reduced for lower SNR of the received signal per RF chain.

5. CONCLUSION

We developed a low-complexity PoC platform for a fully-digital JCR sounding testbed with SIMO functionality and low-resolution ADCs per RF chain at 73 GHz with 2 GHz bandwidth. For precise radar performance evaluation, we conducted experiments using our JCR measurement platform and a corner reflector in the indoor setting. Experimental results showed that the GAMP processing provided an enhanced channel estimate with a larger dynamic range as compared to the FFT-based processing. The radar image estimated using 1-bit ADC emulation and GAMP processing detected the corner reflector without any distortion as compared to the high-resolution ADC employed in our mmWave testbed. For a threshold of -35 dB in the normalized radar image for 1-bit ADC at an SNR of 5, there was no false detection observed in the range-angle domain. The results in this paper demonstrate the high-resolution capability with a wide field of view of our low-complexity wideband fully-digital JCR testbed. In our future work, we will characterize the JCR performance with 1-bit ADC in complex target scenarios and will benchmark our JCR platform with other radar prototyping platforms.

6. REFERENCES

[1] K. V. Mishra, M. R. Bhavani Shankar, V. Koivunen, B. Ottersten, and S. A. Vorobyov, "Toward millimeter-wave joint radar communications: A signal processing perspective," *IEEE Signal Process. Mag.*, vol. 36, no. 5, pp. 100–114, Sep. 2019.

[2] B. Le, T. W. Rondeau, J. H. Reed, and C. W. Bostian, "Analog-to-digital converters," *IEEE Signal Process. Mag.*, vol. 22, no. 6, pp. 69–77, Nov. 2005.

[3] J. Lien, N. Gillian, M. E. Karagozler, P. Amihood, C. Schwesig, E. Olson, H. Raja, and I. Poupyrev, "Soli: Ubiquitous gesture sensing with millimeter wave radar," *ACM Trans. on Graph.*, vol. 35, no. 4, p. 142, Jul. 2016.

[4] J. Choi, V. Va, N. Gonzalez-Prelcic, R. Daniels, C. R. Bhat, and R. W. Heath, "Millimeter-wave vehicular communication to support massive automotive sensing," *IEEE Commun. Mag.*, vol. 54, no. 12, pp. 160–167, Dec. 2016.

[5] J. Liu, Z. Luo, and X. Xiong, "Low-resolution ADCs for wireless communication: A comprehensive survey," *IEEE Access*, vol. 7, pp. 91 291–91 324, Jul. 2019.

[6] A. Mezghani, F. Antreich, and J. A. Nossek, "Multiple parameter estimation with quantized channel output," in *Proc. Int. ITG Workshop on Smart Antennas*, Feb. 2010, pp. 143–150.

[7] J. Mo, P. Schniter, and R. W. Heath, "Channel estimation in broadband millimeter wave MIMO systems with few-bit ADCs," *IEEE Trans. on Signal Process.*, vol. 66, no. 5, pp. 1141–1154, Mar. 2018.

[8] S. J. Zahabi, M. M. Naghsh, M. Modarres-Hashemi, and J. Li, "Compressive pulse-Doppler radar sensing via 1-bit sampling with time-varying threshold," in *Proc. IEEE Int. Conf. on Acoust., Speech and Signal Process.*, Mar. 2017, pp. 3419–3423.

[9] S. J. Zahabi, M. M. Naghsh, M. Modarres-Hashemi, and J. Li, "One-bit compressive radar sensing in the presence of clutter," *IEEE Trans. on Aerosp. and Electronic Syst.*, pp. 1–1, May 2019.

[10] P. Kumari, K. U. Mazher, A. Mezghani, and R. W. Heath, "Low resolution sampling for joint millimeter-wave MIMO communication-radar," in *Proc. IEEE Statistical Signal Process. Workshop*, Jun. 2018, pp. 193–197.

[11] K. U. Mazher, A. Mezghani, and R. W. Heath, "Low resolution millimeter wave radar: Bounds and performance," in *Proc. Asilomar Conf. on Signals, Syst., and Comput.*, Oct. 2018, pp. 554–558.

[12] P. Kumari, A. Mezghani, and R. W. Heath Jr, "A MIMO joint communication-radar measurement platform at the millimeter-wave band," *Accepted in Eur. Conf. in Antenna Propag.*, Dec. 2019.

[13] P. Kumari, J. Choi, N. González-Prelcic, and R. W. Heath, "IEEE 802.11ad-based radar: An approach to joint vehicular communication-radar system," *IEEE Trans. Veh. Technol.*, vol. 67, no. 4, pp. 3012–3027, Apr. 2018.

[14] "Wireless LAN Medium Access Control (MAC) and Physical Layer (PHY) Specifications. Amendment 3: Enhancements for Very High Throughput in the 60 GHz Band," *IEEE Std. 802.11ad*, 2012.

[15] M. Cudak, T. Kovarik, T. A. Thomas, A. Ghosh, Y. Kishiyama, and T. Nakamura, "Experimental mm wave 5G cellular system," in *Proc. IEEE Globecom Workshops*, Dec. 2014, pp. 377–381.

[16] W. U. Bajwa, J. Haupt, A. M. Sayeed, and R. Nowak, "Compressed channel sensing: A new approach to estimating sparse multipath channels," *Proc. of the IEEE*, vol. 98, no. 6, pp. 1058–1076, Jun. 2010.

[17] J. Singh, S. Ponnuru, and U. Madhow, "Multi-gigabit communication: the ADC bottleneck," in *Proc. IEEE Int. Conf. on Ultra-Wideband*, Sep. 2009, pp. 22–27.

[18] S. Rangan, "Generalized approximate message passing for estimation with random linear mixing," in *Proc. IEEE Int. Symp. on Inf. Theory*, Jul. 2011, pp. 2168–2172.

[19] A. Mezghani and J. A. Nossek, "Efficient reconstruction of sparse vectors from quantized observations," in *Proc. Int. ITG Workshop on Smart Antennas*, Mar. 2012, pp. 193–200.

[20] J. P. Vila and P. Schniter, "Expectation-maximization Gaussian-mixture approximate message passing," *IEEE Trans. on Signal Process.*, vol. 61, no. 19, pp. 4658–4672, Oct. 2013.